

Ultracold Neutron Storage Simulation Using the
Kassiopeia Software Package

by
Zachary Bogorad



Submitted to the Department of Physics
in partial fulfillment of the requirements for the degree of
Bachelor of Science in Physics

at the

MASSACHUSETTS INSTITUTE OF TECHNOLOGY

June 2019

© Massachusetts Institute of Technology 2019. All rights reserved.

Signature redacted

Author

Department of Physics
May 10, 2019

Signature redacted

Certified by


Joseph A. Formaggio
Professor of Physics
Thesis Supervisor

Signature redacted

Accepted by

Nergis Mavalvala
Associate Department Head, Department of Physics

Ultracold Neutron Storage Simulation Using the Kassiopeia Software Package

by

Zachary Bogorad

Submitted to the Department of Physics
on May 10, 2019, in partial fulfillment of the
requirements for the degree of
Bachelor of Science in Physics

Abstract

The Kassiopeia software package was originally developed to simulate electromagnetic fields and charged particle trajectories for neutrino mass measurement experiments. Recent additions to Kassiopeia also allow it to simulate neutral particle trajectories in magnetic fields based on their magnetic moments. Two different methods were implemented: an exact method that can work for arbitrary fields and an adiabatic method that is limited to slowly-varying fields but is much faster for large precession frequencies. Additional interactions to simulate reflection of ultracold neutrons from material walls and to allow spin-flip pulses were also added. These tools were used to simulate neutron precession in the Paul Scherrer Institute's neutron electric dipole moment experiment and predict the values of the longitudinal and transverse relaxation times as well as the trapping lifetime. All three parameters are found to closely match the experimentally determined values when simulated with both the exact and adiabatic methods, confirming that Kassiopeia is able to accurately simulate neutral particles. This opens the door for future uses of Kassiopeia to prototype the next generation of atomic traps and ultracold neutron experiments.

Thesis Supervisor: Joseph A. Formaggio
Title: Professor of Physics

Acknowledgments

I would like to thank Joseph Formaggio for being an invaluable mentor to me for the last several years. I would also like to thank Mathieu Guigue for some helpful discussion, as well as to acknowledge the KATRIN and Project 8 collaborations for their support of this project. This work was supported by the MIT Undergraduate Research Opportunities Program, by the Department of Energy Office of Nuclear Physics under award number DE-SC0011091, and by SERI-FCS under award number 2015.0594. Other allied works were supported by Sigma Xi under grant number G2017100190747806.

Contents

1	Introduction	15
2	The PSI nEDM Experiment	17
2.1	The Neutron Precession Chamber	19
3	Equations of Motion for Spin	21
3.1	Exact Equations of Motion	21
3.2	Adiabatic Equations of Motion	22
4	Surface Interactions of Ultracold Neutrons	25
5	The Structure of Kassiopeia	29
5.1	Initialization	29
5.2	Simulation	31
6	Implementation of the Simulation	33
6.1	Additional Kassiopeia Features	33
6.2	Analysis	35
7	Results & Discussion	37
7.1	The Longitudinal Relaxation Time T_1	37
7.2	The Transverse Relaxation Time T_2	38
7.3	The Effective Trap Lifetime τ	38
7.4	Summary of Results and Discussion	39

8 Other Applications	41
A XML Bindings for New Kassiopia Features	43
A.1 Generators	43
A.2 Trajectories	45
A.3 Interactions	46
A.4 Output	46
B Figures	49
C Tables	57

List of Figures

B-1	A plot of the z component of the magnetic field at the center (length-wise) of the PSI precession chamber in one of the field configurations. The larger dots are the field values provided to us (measured in [39]) while the smaller dots are our interpolated values. The $\mathcal{O}(1 \text{ nT})$ variations in the field are typical of the entire trap, both configurations, and all three components.	49
B-2	A VTK image of three neutrons tracked for 1 second inside of the PSI precession chamber. Colors correspond to kinetic energies, with higher energies at the blue end of the spectrum. Note the approximately specular reflections and the slight curvature in the tracks induced by gravity.	50
B-3	The vectors used to define the adiabatic coordinates m and ϕ from the spin vector \mathbf{s} in (3.5).	50
B-4	Plots of the exact (left, see (4.2)) and approximate (right, see (4.4b)) outgoing angle distributions for a UCN incident on a surface with $wk = 2.4$ (typical for our simulations) and an angle to the surface normal of $\pi/7$. Note how the two distributions are reasonably similar, though the approximation is rough since $wk \sim 1$. This was acceptable for us since there was no reason for our simulation results to depend strongly on the exact angular distribution function.	51

- B-5 A comparison of neutron spin angles around the local magnetic field (in the coordinate system defined by (3.5)), including an adiabatic trajectory with an integration time step of $100 \mu\text{s}$ and exact trajectories with time steps of 5, 10, and $20 \mu\text{s}$. These were run in a version of the neutron precession chamber described in this work, but with the magnetic field scaled up by a factor of 1000, resulting in a precession frequency of approximately 30 MHz. As this comparison shows, the adiabatic trajectory agrees well with the exact trajectory at a much shorter step size, but the exact trajectory rapidly loses accuracy as the step size approaches the precession period of $33 \mu\text{s}$. Note that the plot necessarily suffers from aliasing, but sampling was done simultaneously so that points at the same time can be compared. 52
- B-6 The distribution of UCN energies after 300 seconds, using adiabatic simulations of neutrons in one field configuration. Note that the average energy is now far below the initial 150 neV, and in fact a sharp cutoff around the real part of the optical potential (approximately 150 neV) is apparent. 53
- B-7 A comparison of the fractional remaining longitudinal polarization measured at PSI (Figure 5.18 in [23], p.114) with the results of our adiabatic and exact simulations, including 1σ confidence intervals for the simulations and 1σ error bars for the experimental data. The x-axis labels are hidden as the PSI data sets are not yet published. Here, a 0.95 relative polarization corresponds to an average spin along the z-axis equal to 0.95 times the initial average spin along the z-axis. Each data set averages over the two field configurations and over initially aligned and anti-aligned neutrons. We see good agreement over the entire period; the deviation of the exact data at long times is not statistically significant. 54

- B-8 A comparison of the fractional remaining transverse polarization measured at PSI (Figure 2.38 in [42], p.73) with the results of our adiabatic and exact simulations, including 1σ confidence intervals for the simulations and 1σ error bars for the experimental data. The x-axis labels are hidden as the PSI data sets are not yet published. Here, a 0.95 relative polarization corresponds to an average spin along the axis of average precession equal to 0.95 times the initial average spin along the initial polarization axis. Each data set averages over the two field configurations and over two initial spin directions. We see good agreement over the entire period; the deviation of the exact data at long times is not statistically significant. 55
- B-9 A comparison of the fraction of neutrons remaining in the trap measured at PSI (Figure 2.37 in [42], p.72) with the results of our adiabatic and exact simulations, including 1σ confidence intervals for the simulations and 1σ error bars for the experimental data. The x-axis labels are hidden as the PSI data sets are not yet published. Averages for each data set are taken as in Figure B-7 and Figure B-8. Good agreement is seen along the entire PSI data set. Note that the exact data uses a shifted y-axis for visual clarity. The experimental values are arbitrarily normalized as the initial neutron count is not known. 56

List of Tables

C.1 The results of χ^2 testing of our results against the PSI experimental data, including left-sided p-values. Note that ndf=11 for the T1 and T2 measurements and ndf=9 for the lifetime measurements. These values suggest that we are over-estimating our errors, likely due to our results being strongly correlated. The T1 adiabatic lifetime data's disagreement with the experimental data may indicate that our assumed value of η was not correct. 57

Chapter 1

Introduction

At sufficiently low energies, neutrons can be reflected from material walls by the coherent strong interaction [41, 35]. Such neutrons can be stored in material traps, and are termed “ultracold neutrons” (UCNs).

The ability of UCNs to be stored for prolonged periods makes them useful for measuring the neutron lifetime [32]. UCNs can be stored in a trap for various times, and then the remaining number can be counted in order to extract a lifetime. However, the precision of this method is limited by uncertainties in other neutron losses—for example, neutrons leaking out of the trap—so a thorough understanding of neutron dynamics inside the trap is crucial for these measurements. One tool for understanding these dynamics is numerical simulation, which will be the focus of this work.

Precise measurements of the neutron lifetime are interesting in large part because there is currently a large (4σ) experimental discrepancy between the lifetimes obtained from UCN traps and the lifetimes obtained from measuring neutron decay in beams [40, 29]. One possible source of this disagreement is improper understanding of the neutron losses discussed above.

UCNs can also be used to constrain the neutron electric dipole moment, which is related to the strong CP problem and can constrain beyond the Standard Model physics [28, 1, 7]. Currently, the best upper bound on the neutron electric dipole moment (nEDM) comes from measurements on ultracold neutrons, described in [12, 30]. These measurements require extremely fine control over neutron interactions

with fields and surfaces, so they too may benefit from numerical simulation.

To this end, several software packages have previously been used to simulate UCNs, including Geant4 [6], PENTrack [33], STARucn [18] and MCUCN [43]. Some comparisons between these are made in [33, 11]. In this paper, we demonstrate the ability of Kassiopeia [22], a software package originally developed for beta decay experiments, to accurately simulate ultracold neutron storage. We do so by simulating neutron precession in the PSI nEDM experiment and comparing our simulated results to experimental data. The PSI nEDM experiment is an example of an experiment that attempts to use UCNs to measure the nEDM [31, 2, 13].

We begin by describing the PSI nEDM experiment, which we simulated using Kassiopeia, in Chapter 2. We next discuss two sets of equations of motion that can be used to describe the time evolution of neutrons in Chapter 3. We then consider the interactions of neutrons with trap surfaces in Chapter 4. Next, we describe the general structure of Kassiopeia in Chapter 5 before discussing our implementation of a UCN simulation in Chapter 6. In Chapter 7, we describe our results. Finally, we consider possible future uses of spin simulation in Kassiopeia in Chapter 8.

Chapter 2

The PSI nEDM Experiment

The general principle of experiments that aim to measure the nEDM is to compare the Larmor precession frequency of neutrons in both magnetic and electric fields when those fields are oriented in the same direction, and when they are oriented in opposite directions. The external magnetic field will contribute a relatively large amount to the precession frequency, since the neutron has a magnetic moment on the order of a nuclear magneton. However, if the neutron also has a small electric dipole moment, that will contribute to the precession frequency, either increasing or decreasing it depending on whether the fields are aligned or anti-aligned. Since UCNs can be stored for long periods, they are suitable for measuring small differences in the precession frequency between these relative field alignments.

The PSI nEDM experiment [31, 2, 13] was one experiment that looked for an nEDM using UCNs. Neutrons were first produced via spallation [26, 38]. A proton beam was directed at a spallation target consisting of 760 Zirconium alloy tubes filled with lead, resulting in the release of hot neutrons.

These neutrons were next cooled by passing through the heavy water (D_2O) at 300 K above the spallation target [26]. A chamber of solid deuterium at 5 K then cooled these neutrons to become UCNs via phonon interactions [8]. While the neutrons would regain approximately 100 neV upon leaving this D_2 crystal, this could be compensated for by gravity by extracting the neutrons approximately 100 cm higher.

A single neutron polarization was then selected using a large, fixed (5 T) magnetic

field, and adiabatic precession was used to achieve the desired initial spin state (up or down, depending on the run). The UCNs were then deflected into a cylindrical precession chamber.

After 28 seconds of filling the chamber, the chamber was closed off, leaving the neutrons to precess inside the chamber. This precession is what was simulated for this work. The chamber is described in detail in the next section, 2.1, but we will first summarize the experimental procedure.

Two homogeneous fields were created within the chamber: an electric field of roughly 111 kV/cm, and a magnetic field of approximately 1 μ T. Both fields could be oriented in either direction along the cylinder axis.

Immediately after the chamber was filled, neutrons' spins would be either aligned or anti-aligned with the chamber's magnetic field. In some runs (see section 6.2), a $\pi/2$ pulse was then used to orient those spins perpendicular to that field, resulting in precession. Note that a nEDM would result in different precession rates depending on the relative orientation of the electric and magnetic fields. At the end of the storage time, another $\pi/2$ pulse was applied if needed.

Neutrons were then released from the precession chamber, and guided to a spin detection system, described in [4]. Measurements of the fraction of neutron spins in the up (or down) state would then allow calculation of the precession rate. A detection of a difference in rate between the relative field orientations would allow calculation of an nEDM, though no significant difference was observed. This process was repeated 50,000 times.

To reduce errors from fluctuations in the magnetic field, the PSI nEDM experiment simultaneously measured precession of mercury atoms (^{199}Hg) in a cohabiting magnetometer setup: any changes in the magnetic field would be reflected in changes in the mercury's precession, so measurements of the mercury's precession (in the same manner as for UCNs) allowed for compensation for this effect.

2.1 The Neutron Precession Chamber

Since we simulated only the evolution of neutrons within the precession chamber for this work, we next describe the relevant parameters of the precession chamber and its contents, as they were implemented in our simulation.

The PSI neutron precession chamber was a cylinder of radius 23.5 cm and height 12 cm. The interior rounded surface was primarily deuterated polystyrene (dPS), with small windows of deuterated polyethylene (dPE), while the two flat ends of the cylinder (the electrodes) were covered in diamond-like carbon (DLC). For purposes of our simulation, the entire surface was assumed to be dPS, since it is the primary surface cover and any changes associated with including dPE and DLC are likely to be smaller than the uncertainties in the values described below.

For our purposes, neutrons were assumed to begin at the bottom surface of the precession chamber. While this is not accurate, the neutrons are sufficiently fast that this should not affect the results significantly.

As noted above, the interior of the precession chamber contained an approximately homogeneous magnetic field of roughly $1 \mu\text{T}$. This field had known, order-1 nT deviations along each axis, however. A map of these deviations (measured in [39]) at discrete points was provided to us and we used a combination of natural neighbors interpolation (to reach a rectilinear lattice) and cubic interpolation (within lattice cells) to estimate the magnetic field throughout the precession chamber. A plot of both the original field values and our interpolated values in one region of the trap is shown in Figure B-1. Since our simulation assumes a zero nEDM, the electric fields were not included in simulations since they would have no effect.

Neutron kinetic energies were generated from a Gaussian distribution of mean 150 neV and standard deviation 50 neV. This is a higher energy distribution than the energy distribution estimated by PSI [5], but we found that the estimated distribution did not fit the data as well. We will return to this point in Chapter 4.

Three example tracks inside of the simulated PSI precession chamber are shown in Figure B-2.

Chapter 3

Equations of Motion for Spin

3.1 Exact Equations of Motion

The relativistic generalization of a classical spin is the four-vector $S = (S_0, \mathbf{S})$ given by, for a particle with classical spin \mathbf{s} , velocity $\mathbf{v} = \beta c$, and Lorentz factor Γ (to avoid confusion with the gyromagnetic ratio γ) [25],

$$S_0 = \Gamma \beta \cdot \mathbf{s} \quad (3.1a)$$

$$\mathbf{S} = \mathbf{s} + \frac{\Gamma^2}{\Gamma + 1} (\beta \cdot \mathbf{s}) \beta. \quad (3.1b)$$

The equations of motion for a relativistic spin with 4-velocity U^α in fields $F^{\mu\nu}$, using the particle's proper time τ , are given by the BMT equation:

$$\frac{\partial S^\alpha}{\partial \tau} = \frac{\gamma}{c} \left[F^{\alpha\beta} S_\beta + \frac{1}{c^2} U^\alpha (S_\lambda F^{\lambda\mu} U_\mu) \right] - \frac{1}{c^2} U^\alpha \left(S_\lambda \frac{\partial U^\lambda}{\partial \tau} \right). \quad (3.2)$$

In this work, we will use only the usual, non-relativistic form of the force on a magnetic dipole, as this is the form implemented in our simulation package:

$$\mathbf{F} = \nabla(\gamma \mathbf{s} \cdot \mathbf{B}). \quad (3.3)$$

At first, this may appear to be inconsistent with our use of the relativistic spin equa-

tions of motion above. However, due to the smallness of both the neutron magnetic moment and the magnetic fields we will be considering, the magnetic dipole force is itself a tiny correction to the neutron equations of motion, which are dominated by gravity and surface interactions. As a result, relativistic force corrections for our non-relativistic neutrons are not significant. By contrast, the relativistic corrections to spin evolution are more significant, since spin is not affected by gravity and is generally not affected by the surface interactions (see Chapter 4).

These exact spin equations of motion are completely general, except for the assumption that relativistic corrections to the magnetic dipole force term are irrelevant. However, the step size for numerically integrating these equations of motion is limited by the precession rate of the spins, $\gamma|\mathbf{B}|$. This is typically fast relative to other timescales of a particle's motion, which can make the exact spin tracking method impractically slow for experiments with long timescales.

3.2 Adiabatic Equations of Motion

We next consider an adiabatic form for the spin equations of motion. In this form, it is easiest to work with a different set of spin coordinates: an aligned spin m that gives the component of the spin along the magnetic field at the particle's position, and a spin angle ϕ that gives the orientation of the spin around that field. This spin angle is defined with respect to two unit vectors orthogonal to the local magnetic field, \mathbf{e}_1 and \mathbf{e}_2 , defined, for a magnetic field $\mathbf{B} = (B_x, B_y, B_z)$ in laboratory coordinates, as:

$$\mathbf{e}_1 := (B_z, 0, -B_x)/\sqrt{B_x^2 + B_z^2} \quad (3.4a)$$

$$\mathbf{e}_2 := \mathbf{B} \times \mathbf{e}_1/|\mathbf{B}|. \quad (3.4b)$$

Given these axes, ϕ gives the angle of the projection of the spin into the plane perpendicular to \mathbf{B} away from \mathbf{e}_1 , in the direction of \mathbf{e}_2 :

$$\mathbf{s} = (s^2 - m^2)^{1/2}(\mathbf{e}_1 \cos \phi + \mathbf{e}_2 \sin \phi) + m\mathbf{B}/|\mathbf{B}| \quad (3.5)$$

The relationship between these vectors is illustrated in Figure B-3.

These two parameters, m and ϕ , along with the position x , then give the adiabatic spin equations of motion (excluding contributions independent of spin) [27]:

$$\frac{M}{\hbar} \dot{\mathbf{x}} = \gamma m \nabla |\mathbf{B}| + \gamma |\mathbf{B}| (s^2 - m^2)^{1/2} \nabla \mathbf{b} \cdot \mathbf{c} \quad (3.6a)$$

$$\frac{\dot{m}}{s} = (s^2 - m^2)^{1/2} (\dot{\mathbf{x}} \cdot \nabla \mathbf{b} \cdot \mathbf{c}) \quad (3.6b)$$

$$\dot{\phi} = -\gamma |\mathbf{B}| - \dot{\mathbf{x}} \cdot \mathbf{A} - \frac{sm}{(s^2 - m^2)^{1/2}} (\dot{\mathbf{x}} \cdot \nabla \mathbf{b} \cdot \mathbf{a}) \quad (3.6c)$$

where x is position, γ is the particle's gyromagnetic ratio, M is its mass, s is the magnitude of its total spin, and we have defined

$$\mathbf{a} = -\mathbf{e}_1 \cos \phi + \mathbf{e}_2 \sin \phi \quad (3.7a)$$

$$\mathbf{b} = \mathbf{B}/|\mathbf{B}| \quad (3.7b)$$

$$\mathbf{c} = \mathbf{e}_1 \cos \phi + \mathbf{e}_2 \sin \phi \quad (3.7c)$$

$$\mathbf{A} = (\nabla \mathbf{e}_1) \cdot \mathbf{e}_2. \quad (3.7d)$$

These adiabatic equations of motion are accurate when particles are non-relativistic and spin precession is fast compared to the rate at which the field at the particle's location changes. Assuming the spin precession rate is dominated by the first term $\gamma |\mathbf{B}|$, this requires $\gamma |\mathbf{B}| \gg |\dot{\mathbf{x}} \cdot \nabla \mathbf{B}|/|\mathbf{B}|$, which should hold for all applications discussed in this work. During a single integration time step, the exact equations of motion require the spin to rotate by much less than a radian, so the left-hand side of that inequality approximately sets the maximum step size for exact spin integration. The adiabatic equations of motion can handle large rotations per time step but assume a constant field during the step, so the right-hand side limits the step size for adiabatic spin integration. In this limit, therefore, the adiabatic approach can be much faster.

Figure B-2 shows three example simulated neutron tracks inside of the PSI precession chamber. These were calculated using the adiabatic equations of motion. We will discuss the details of this simulation in Chapter 6.

Chapter 4

Surface Interactions of Ultracold Neutrons

UCN reflections from surfaces are described by three features: the depolarization probability, the reflection probability, and the distribution of outgoing angles for reflected neutrons. The first two are described in [17], while the third is described in [10]. We will summarize these and discuss our estimates of the associated parameters.

The UCN depolarization probability is the simplest to describe, and is given by a constant β . For dPS, this is known very roughly as $\beta \sim 10^{-6} - 10^{-5}$ [17], and again a range of values for DLC are given in [9].

The UCN reflection probability at an energy E and incident angle to the surface normal θ is given by

$$P(R) = 1 - \eta \left(\frac{E_{\perp}}{V_f - E_{\perp}} \right)^{1/2} \quad (4.1)$$

where $E_{\perp} = E \cos^2 \theta$ is the component of energy from normal momentum, V_f is the real part of the surface's optical potential, and η is another constant of the surface. For dPS, these values are known only approximately, with $\eta \sim (1 - 3) \times 10^{-4}$ and $V_f \sim 1.6 \times 10^{-7}$ eV [17], while a range of values for DLC were found in [9].

The distribution of outgoing angles for UCNs is more complex. Detailed theoretical treatments can be found in [10, 36]. Since the behavior of UCNs in the precession chamber should not depend significantly on the exact angular distribution, we derive

an approximate form. We start from the microroughness model result which, up to a normalization constant, can be modeled as:

$$p(\theta_f, \Phi_f) \propto |S(\theta_f)|^2 \exp \left[-\frac{(wk)^2}{2} (\sin^2 \theta_i + \sin^2 \theta_f - 2 \sin \theta_i \sin \theta_f \cos \Phi_f) \right] \quad (4.2)$$

Here, θ_i and θ_f are the incident and outgoing angles to the normal, ϕ_f is the change in direction around the normal, w is the surface roughness, k is the neutron wave vector, and

$$|S(\theta_f)| = \left| \frac{2 \cos \theta_f}{\cos \theta_f + \sqrt{\cos^2 \theta_f - k_c^2/k^2}} \right| \quad (4.3a)$$

$$= 2k \cos \theta_f / k_c \quad (4.3b)$$

where $k_c = \sqrt{2mV_f/\hbar}$ is the wave number corresponding to the optical potential.

We are interested only in neutrons with $k < k_c$, since higher-energy neutrons quickly escape the precession chamber. Then

$$p(\theta_f, \Phi_f) \propto \cos^2 \theta_f \exp \left[-\frac{1}{2} (wk)^2 (\sin \theta_i - \sin \theta_f)^2 + (wk)^2 \sin^2 \theta_i (\cos \Phi_f - 1) \right] \quad (4.4a)$$

$$\approx (1 - \tan \theta_i \Delta\theta) \exp \left[-\frac{(wk)^2}{2} \cos^2 \theta_i \Delta\theta^2 - \frac{(wk)^2}{2} \sin^2 \theta_i \Phi_f^2 \right] \quad (4.4b)$$

where we defined $\Delta\theta = \theta_f - \theta_i$. This gives a simple approximate distribution of outgoing angles that can be efficiently sampled.

Note that this derivation assumes that the change in incident and outgoing angles is small. This is a rough approximation in our case, but we found that our simulations were insensitive to the exact parameters of the reflected distribution, so this should not significantly affect our results.

For our simulations, we used $\beta = 6 \times 10^{-6}$, $\eta = 1 \times 10^{-4}$, $V_f = 150$ neV, and $w = 30$ nm, which were consistent with the available estimated ranges of each value (see [37, 20] for measurements of w). The first two parameters were tuned so as to be most consistent with PSI's data. In the future, it might be possible to use our

simulations as a means of actually determining these values, but in this work we only estimated these up to an $\mathcal{O}(1)$ factor.

Note that these $\mathcal{O}(1)$ differences may account for the disagreement with PSI's estimated energy distribution that we mentioned in Chapter 2. Further simulation work, as well as improved characterization of the experiment and the relevant surfaces, is needed in order to resolve this disagreement.

Chapter 5

The Structure of Kassiopeia

Kassiopeia was created as a combined field solver and particle tracker for the KATRIN collaboration [22]. It is developed in C++ using a modular design that allows it to be adapted to various applications using different field solvers, equations of motion and interactions. The standard distribution, available at <https://github.com/KATRIN-Experiment/Kassiopeia>, implements a variety of these features already, and Kassiopeia is designed for easy development of additional modules for future applications. Individual simulations can then be configured using an Extensible Markup Language (XML) file.

The operation of Kassiopeia can be roughly divided into two stages: an initialization stage, in which the software processes the particles' environment, independent of the particular particles being simulated; and a simulation stage, in which those particles are generated, their motion is numerically simulated, and results are output.

5.1 Initialization

During the initialization stage, Kassiopeia processes the static geometry within which particles will be simulated, and calculates electric and magnetic fields within it.

The environmental geometry is specified in the input XML file in a nested manner. The overall simulation space can contain subspaces, which can themselves have further subspaces. Different spaces can be given different properties: for example, a

particular space may have an additional interaction (discussed in the next section, 5.2) to simulate scattering from a gas within that space.

Spaces may be given a variety of built-in shapes, in particular rectangular prisms or cylinders. Alternatively, the user may define additional shapes within the XML file using extrusions or rotations of polylines. Once a shape is defined, spaces may be described using translations and rotations of these shapes.

The user may then add surfaces to any spaces. Similarly to spaces, surfaces may be defined using one of several built-in shapes, including planes and disks, or user-defined surface shapes may be created using polylines. Again, shapes may then be translated or rotated as needed.

Like spaces, surfaces may have associated interactions that occur when particles reach them. For example, surfaces may be given reflection and transmission probabilities, which may depend on properties of the incoming particle. Surfaces may also be assigned electrical properties (e.g. currents) that will be used for electromagnetic field calculation. Some common electromagnetic elements, most notably cylindrical solenoids, are built-in, while others may again be defined by the user.

Once the geometry for a simulation is set, Kassiopeia can generate electric and magnetic fields within the environment in one of three ways: fields may be calculated from the electric and magnetic properties assigned to the geometry; they may be defined analytically; or they can be computed elsewhere and imported.

Kassiopeia has several implemented methods to calculate the electromagnetic fields associated with a particular current geometry. Magnetic fields can be calculated using zonal harmonic expansions [19] or the fast multipole method [15], while electric fields can be computed using the boundary element method [19].

For this work, we instead imported the magnetic fields measured by PSI into Kassiopeia. Externally computed fields may be imported using the VTK Image Data (.vti) format [34], specifying the electric or magnetic field on the points of a Cartesian lattice. Fields between these points are then estimated using one of several interpolation techniques; for this work we used cubic interpolation. A plot of both the measured field values and the lattice of field values we passed to Kassiopeia is

shown in Figure B-1.

5.2 Simulation

After constructing the environment, Kassiopeia can begin simulating particle evolution within that space. In the language of Kassiopeia, one “run” of the software can involve one or more “events”, each of which can involve one more “tracks”, which in turn typically involve many “steps”.

Runs in Kassiopeia constitute a single execution of the software. This is the level at which Kassiopeia can be parallelized: though most of Kassiopeia’s functions do not implement multi-threading, simulations can be run in parallel using multiple simultaneous executions of the software, and the outputs can be combined afterwards.

Within a run, each event consists of one or more causally connected particle tracks. A simple example of an event is a decay process, which might produce one or more particles that need to be simulated. Initial events can be created using “generators,” which create a particle with user-specified properties (or properties from a specified distribution). A wide variety of generators are built into Kassiopeia. Further events may be created by interactions, such as scattering processes.

Each track in Kassiopeia consists of the time evolution of a particle using a single set of simulation parameters. This may be the entire evolution of the particle, or it may be only a part of that evolution: tracks can end at a surface and then a new track can continue to simulate the same particle beyond that surface, but using a different numerical method, for example.

Finally, each step in Kassiopeia is essentially an integration step of the equations of motion, but with a number of additional features. In particular, during each step, Kassiopeia not only propagates the particle state, but also checks for surface crossings, interactions, and termination conditions.

A large fraction of output is typically also done at the step level, though the collective properties of, for example, events may be output as well. Kassiopeia outputs simulation results using the ROOT (`.root`) file format [16].

Chapter 6

Implementation of the Simulation

6.1 Additional Kassiopeia Features

The Kassiopeia modules responsible for solving particles' equations of motion are called "trajectories." Different trajectories include different terms in the equations of motion and use different representations of particle states.

Early versions of Kassiopeia included two main trajectory modules: an exact trajectory module, which describes particles via their position and momentum in laboratory coordinates and is limited only by the integration step size, and an adiabatic trajectory module, which calculates and records particles' position and motion around the magnetic field lines that they adiabatically follow at sufficiently low energies.

Both of these modules implemented equations of motion that assumed a non-zero particle charge, which prevented Kassiopeia from simulating other particles of interest, such as neutrons or neutral atoms. To remedy this, two new trajectory modules were added to Kassiopeia: an exact spin trajectory and an adiabatic spin trajectory, which implemented the exact and adiabatic spin equations of motion, respectively (see Chapter 3). Both modules describe particles' position and momentum in laboratory coordinates, as in the original exact trajectory, but then include the additional terms due to particles' magnetic moments, determined by their spins. These additional terms are potentially the only non-zero terms in the equations of motion for neutral particles.

A comparison of the outputs from the adiabatic and exact trajectories is shown in Figure B-5. Note that the exact trajectory becomes increasingly inaccurate as the integration time approaches the precession period $33 \mu\text{s}$, even for 10 ms tracks.

We noted in Chapter 3 that the adiabatic spin equations of motion can typically be integrated much more quickly than the exact spin equations of motion. In the contest of full trajectories (including the equations of motion for position), however, there may be other limitations on the step size that prevent this from being the case. In particular, for the ultracold neutron tracking described in this work, weak magnetic fields mean that the limiting factor on the time step is error in position, not spin, so adiabatic and exact spin tracking require similar computation time. As a result, in this work we were able to validate both methods.

Alongside these two new trajectories, we introduced new generators to create particles with spin. Two generators were introduced to accommodate different initial conditions: an absolute spin generator, which initializes spin in the global (x,y,z) coordinates; and a relative spin generator, which initializes spin relative to the local magnetic field.

As is standard for Kassiopeia’s generators, both can be tied to a variety of distributions to actually choose those spin values (also called “generators” in Kassiopeia). Most typically, initial spins can be fixed by the user in the XML input, or can be drawn from a uniform spherical distribution. The latter can be restricted to only some azimuthal and/or longitudinal angles.

The other major addition we made to Kassiopeia was the introduction of two new interactions for simulating UCNs. The first is the UCN reflection process described in Chapter 4. This allows for user-specified values of the β , η , V_f and w parameters described therein.

We also added a spin rotation interaction to imitate the effect of the $\pi/2$ pulses used by the PSI nEDM experiment, though it can accommodate any rotation angle. This was implemented as a space interaction, so it can be applied to all or part of the experimental volume, as described in Chapter 5. At a particular time, the interaction rotates a particle’s spin about the y-axis by a user-specified angle.

Realistic spin rotation pulses take finite time, but for our purposes this interaction was instant as this was far easier to implement and use in Kassiopeia, and we do not expect this to have any significant impact on our results. For the final simulations, this interaction was actually not used at all to simplify the analysis. Instead, when needed, particles were generated in their post-rotation states and then final rotations were applied during data analysis.

6.2 Analysis

Our data analysis was conducted using PyROOT [16]. Our goal was to extract three parameters: the effective lifetime of neutrons within the trap, and the relaxation times T1 and T2.

The longitudinal relaxation time, T1, is the time constant of the decay of average polarization for neutrons with initial spins that are either aligned or anti-aligned relative to the local magnetic field. In particular, it is the time constant for decay towards the thermal distribution of aligned spin. It should be noted that, even for ultracold neutrons, the μT -order magnetic fields in the precession chamber do not significantly affect neutron energies since $\mu_N |\mathbf{B}|$ is far less than the kinetic energy, so the ultimate thermal evolution of neutrons in the chamber is towards an essentially uniform distribution of spins. On a microscopic level, longitudinal relaxation is associated with inhomogeneities of the magnetic field, and with depolarization due to reflections.

Since the adiabatic equation of motion (3.6b) for fully aligned or anti-aligned spins always gives a zero derivative of the aligned spin, our simulations instead started spins at 1° or 179° to the magnetic field, though we found that any angle up to a few degrees led to indistinguishable results, as the dominant contribution to T1 came from reflection depolarization.

The transverse relaxation time, T2, is the time constant of the decay of average polarization for neutrons with initial spins that are aligned along an axis perpendicular to the local magnetic field. The dominant contribution to transverse relaxation

of neutrons in the precession chamber is the variation in the magnetic field over the trap volume. Note that spin-spin interactions, which may be the dominant contribution to T2 in other contexts, should not be significant for neutrons and cannot be implemented in Kassiopeia, which tracks particles one at a time.

In PSI's T2 measurements, neutrons began with polarizations aligned or anti-aligned with the magnetic field and then T2 was measured between two $\pi/2$ pulses that rotated them into and out of the perpendicular plane. While ideal spin rotating pulses are implemented in Kassiopeia, they were not used for this simulation since it was simpler to simulate starting from after the initial pulse, and to apply the final pulse during data analysis.

Extracting T1 from the Kassiopeia was straightforward: the fraction of spins aligned or anti-aligned with the local magnetic field was output at every step. T2 however, is slightly more complicated to estimate, due to the need for the $\pi/2$ pulses. In the actual experiment, the timing of the second $\pi/2$ pulse was optimized to maximize the fraction of neutrons restored along the magnetic field. In our analysis, we instead varied the axis around which the $\pi/2$ rotation occurred at fixed times, using the axis that maximized the resulting polarization.

Since neutron reflection from material surfaces is not guaranteed, especially at higher energies (see (4.1)), the effective lifetime of neutrons in the precession chamber is significantly lower than their decay lifetime. Neutrons may also be lost due to holes or other imperfections in a physical trap, which should be included in the estimated value of η .

Lifetime analysis, like T1 analysis, was straightforward, as the number of remaining neutrons at a given time can be read directly from Kassiopeia's output.

A variety of other information can be extracted from our simulations if needed. For example, our simulations can be used to study the evolution of the energy distribution of neutrons within the precession chamber. Figure B-6 shows the energy distribution of remaining neutrons at 300 seconds for particular initial parameters. The decreased average energy and the sharp cutoff at the optical potential are evident.

Chapter 7

Results & Discussion

We compared our simulation’s results with three previously measured parameters of PSI’s precession chamber: the longitudinal relaxation time T_1 [23], the transverse relaxation time T_2 [42], and the effective trap lifetime τ including neutron decay and wall losses [23].

A total of 17280 neutrons were simulated up to maximum times of 500 seconds. This was done using 4 parallel `c4.8xlarge` instances of Amazon Elastic Compute Cloud (EC2), or 144 total cores. Kassiopeia does not directly support parallelization of particle tracking, so we instead ran 144 separate simulations of 120 neutrons each and then combined the outputs. This took approximately 2500 CPU-hours, though further optimization is likely possible.

7.1 The Longitudinal Relaxation Time T_1

We simulated 4320 neutrons for 500 seconds using both the adiabatic trajectory with half initially aligned and half initially anti-aligned, and compared our average polarization as a function of time to that obtained by PSI; we did the same with the exact trajectory. Our results can be seen in Figure B-7, where a relative polarization of 1 indicates an average polarization equal to the initial value (± 1 in simulations, but smaller magnitudes in PSI’s experiments).

As Figure B-7 shows, both the adiabatic and exact simulations were able to ac-

curately reproduce the measured longitudinal depolarization rate. Both simulations are within 1σ of the experimental data (using the combined error) until around 350 seconds, and the adiabatic simulations continue to closely match the experiment for the entire run. The apparent discrepancy between the experimental data and the exact trajectory at high times is not statistically significant (see Table C.1).

7.2 The Transverse Relaxation Time T2

We simulated 4320 neutrons for 500 seconds using the adiabatic trajectory and two different initial spin directions perpendicular to the magnetic field; we again did the same with the exact trajectory. We then compared our average polarization as a function of time to that obtained by PSI. Our results can be seen in Figure B-8, with relative polarization defined as for T1, but along the axis corresponding to average precession over that time instead of along the z -axis.

As Figure B-8 shows, both simulations were also able to accurately reproduce the measured transverse depolarization rate. The adiabatic simulation matches all of the experimental values, however the exact simulation results appear to deviate from the data at long times. However, this discrepancy is again not statistically significant (see Table C.1), as our simulation errors are highly correlated: neutrons that deviate significantly from the average polarization (due to depolarization on reflection, for example) are likely to remain in the trap for some time, lowering the average polarization at those later times as well.

7.3 The Effective Trap Lifetime τ

Lifetimes may be extracted from both the T1 and T2 simulations, since the lifetime should be nearly independent of the neutrons' spins in a μT field. The results from both sets of simulations, as well as from PSI's experiments [3], are shown in Figure B-9.

Figure B-9 once again shows good agreement between each of the four simulations

and the experimental data. The adiabatic T1 simulation deviates significantly from the experimental data (see Table C.1), but the lifetime is strongly dependent on the chosen value of η and the initial energy distribution—neither of which is precisely known for the PSI trap—so this discrepancy is not practically significant. Also note that the experimental remaining count data was arbitrarily normalized as the exact number of neutrons at the beginning of each measurement was not known.

7.4 Summary of Results and Discussion

A summary of our simulated data’s agreement to the PSI experimental data is presented in Table C.1, showing generally good agreement. The apparent overestimation of errors is expected to be the result of correlations between our errors at different times: since the polarizations at all times were extracted from the same set of parallel runs, an excessive longitudinal polarization (for example) at a particular time makes excessive longitudinal polarizations at other times more likely. While it may be possible to eliminate this effect using more complicated statistical analysis, this was not necessary for our purpose of validating the simulation. Some of the error is also likely to be associated with the uncertainties in the various reflection parameters discussed in Chapter 4 and in the initial energy distribution of the neutrons.

This good agreement demonstrates that Kassiopeia can reproduce the effective lifetime as well as both decoherence times for neutrons within the PSI precession chamber, confirming that it can accurately simulate neutral particles.

Chapter 8

Other Applications

Having established that Kassiopeia can accurately simulate neutral particles' motion in at least one context, we next consider a few potential future applications of these features.

The application most directly stemming from the simulations in this paper is simulated prototyping of future ultracold neutron experiments. In this work, we simulated neutron precession using a previously measured magnetic field, but Kassiopeia also includes extensive field calculation methods, which can be used to calculate the magnetic fields inside of a trap based on its design [19, 15]. Kassiopeia could therefore be used to estimate the effective lifetime and relaxation times of future ultracold neutron experiments.

Another potential application is simulating tritium storage methods in the Project 8 neutrino mass experiment [21]. We have previously simulated purely magnetic versions of the tritium storage apparatus in order to obtain estimates of necessary currents and effective lifetimes, but development of the final trap configuration is ongoing and further simulation work could be done in this area. Furthermore, one current proposal is to use a combined magneto-gravitational trap instead, which has not been simulated as of writing.

Neutral particle simulation can also be applied to atomic experiments. Experiments such as [14] and [24] use molecular beams to measure the electron's electric dipole moment. Molecules are prepared in particular spin states and then precess

through constant electric and magnetic fields; a dependence of precession on the electric field can indicate an electric dipole moment of the electron. Kassiopeia may be able to simulate molecular evolution within these fields to aid with estimating systematic errors.

Appendix A

XML Bindings for New Kassiopeia Features

In this appendix, we explain some of the XML bindings needed to use the new Kassiopeia features that we created. The official Kassiopeia XML documentation can be found at <http://katrin-experiment.github.io/Kassiopeia/configuration.html> [22]. In this appendix, we will focus only on the new features we added, which are not included in that documentation.

A.1 Generators

We begin with the XML bindings for the relevant generators. Here is an example of the bindings to generate a UCN:

```
<ksgen_generator_composite name="generator_uniform" pid="2112">
  <energy_composite>
    <energy_gauss value_min="10.e-9" value_max="290.e-9"
      value_mean="150.e-9" value_sigma="50.e-9"/>
  </energy_composite>
  <position_cylindrical_composite>
    <r_cylindrical radius_min="0." radius_max="0.23499"/>
    <phi_uniform value_min="0." value_max="360."/>
  </position_cylindrical_composite>
</ksgen_generator_composite>
```

```

    <z_fix value="-0.0599"/>
  </position_cylindrical_composite>
  <time_composite>
    <time_fix value="0."/>
  </time_composite>
  <direction_spherical_composite>
    <theta_spherical angle_min="0." angle_max="180."/>
    <phi_uniform value_min="0." value_max="360."/>
  </direction_spherical_composite>
  <spin_relative_composite>
    <theta_fix value="[angle]"/>
    <phi_uniform value_min="0." value_max="360."/>
  </spin_relative_composite>
</ksgen_generator_composite>

```

The first line in this block marks the beginning of a generator, gives it a name, and specifies that the particle is a neutron (particle ID 2112). The last line signals the end of the generator.

The next section describes how the neutron's energy should be chosen: the energy is pulled from a (truncated) Gaussian distribution, with specified mean, standard deviation, minimum, and maximum.

The following segment is used to choose the neutron's initial position. In this case, the position is chosen in cylindrical coordinates, with a fixed value for z but r and θ chosen from a uniform distribution over a disk. Note that the radial distribution is not uniform, since there is more area at larger radii.

The next few lines specify the neutron's initial time coordinate.

The next section repeat this process for the direction of the initial momentum, which is instead generated in spherical coordinates, with all initial directions made equally likely in this example.

So far, all of these bindings existed in Kassiopeia prior to our work. The next binding is new however: `spin_relative_composite` chooses the initial spin, relative

to the magnetic field at the initial position. This is chosen the same way as the initial direction, except in this case the polar angle is fixed to a variable defined elsewhere (`angle`). However, `theta_spherical` (as above) could be used instead to generate random angles from a sphere (or part of a sphere), or `phi_fix` could be used to specify the initial spin completely.

Initial spins can be specified in global coordinates (independent of the local magnetic field) using `spin_composite` (without the `relative`) instead.

A.2 Trajectories

We next present an example of the bindings for one of our new trajectories:

```
<kstraj_trajectory_exact_spin name="trajectory_adiabatic_spin">
  <interpolator_crk name="interpolator_crk"/>
  <integrator_rk8 name="integrator_rk8"/>
  <term_propagation name="term_propagation"/>
  <term_gravity name="term_gravity" gravity="0. 0. -9.8"/>
  <control_time name="control_time" time="2.e-4"/>
</kstraj_trajectory_exact_spin>
```

Similarly to the generator, the first and last lines establish that this is a trajectory binding and give the trajectory a name. The next two lines specify the numerical methods used to solve the equations of motion and interpolate between points in the solution.

The following two lines specify those equations of motion. The first is the standard set of electromagnetic equations of motion, including the modifications that we made in order to include spin. The second is an additional term we added giving a uniform gravitational acceleration, since this is significant for UCNs but not for most uses of Kassiopeia. Typically, a user should not need to change these lines to use our code, except perhaps to remove the latter if gravity is insignificant.

Finally, the `control_time` line specifies a maximum integration step length.

A.3 Interactions

We now present examples of the two new interactions we added for UCN simulation.

```
<ksint_surface_UCN name="int_surface_UCN" eta="1.e-4"
alpha="5.e-6" real_optical_potential="1.61e-7"
correlation_length="30.e-9"/>
```

This line defines a UCN reflection interaction with the given parameters (see Chapter 4. Note that, like other surface interactions in Kassiopeia, this interaction must also be attached to one or more surfaces elsewhere in the XML in order for it to be active, but this functionality is not specific to our code.

```
<ksint_spin_rotate_y_pulse name="int_spin_rotate_y_pulse_1"
time="5.e-4" angle="90."/>
```

This line defines the spin rotation interaction discussed in Chapter 6, rotating spin around the y-axis by the specified angle at the specified time. The direction of rotation is given by the right hand rule. This is a spatial interaction, so it must be attached to a space elsewhere in the XML and will apply to all particles in that space.

A.4 Output

Finally, we show some of the options for outputting spin-related values from Kassiopeia.

```
<ks_component_group name="component_track_world">
  <component_member name="terminator_name"
field="terminator_name" parent="track"/>
  <component_member name="total_steps"
field="total_steps" parent="track"/>
  <component_member name="initial_time" field="time"
parent="component_track_initial_particle"/>
```

```

<component_member name="initial_position" field="position"
parent="component_track_initial_particle"/>
<component_member name="initial_spin_angle" field="spin_angle"
parent="component_track_initial_particle"/>
<component_member name="final_spin" field="spin"
parent="component_track_final_particle"/>
</ks_component_group>

```

As usual, the first and last lines declare the overall object, in this case simply a collection of output components; as the name suggests, these correspond to track parameters. The next few lines print the terminator name (i.e. the reason the track ended), the track length in steps, the track start time, and the track start position. The following line prints the initial spin angle (i.e. the angle around the local magnetic field, in the coordinate system described in Chapter 3). The next line print the spin 4-vector's last 3 components at the end of the track. One can also print the aligned component of the spin (`aligned_spin`) and the zero component of the spin 4-vector (`spin0`) in similar ways.

Note that, in practice, one should be careful to print the spin only in the coordinate system being used by the chosen trajectory, as the unused coordinates are generally not updated during a track.

A group like this can then be associated with an output command in order to output all of the listed objects; see the general documentation.

```

<ks_component_group name="component_step_world">
  <component_member name="time" field="time"
parent="component_step_final_particle"/>
  <component_member name="position" field="position"
parent="component_step_final_particle"/>
  <component_member name="aligned_spin" field="aligned_spin"
parent="component_step_final_particle"/>
  <component_member name="spin_angle" field="spin_angle"

```

```

    parent="component_step_final_particle"/>
    <component_member name="spin" field="spin"
    parent="component_step_final_particle"/>
</ks_component_group>

```

This group of output components is similar to the above, but corresponds to properties of a step, rather than a track. The first two lines within the group give the time and particle position at that step. The next three give the component of the spin aligned with the local magnetic field, the angle about that field, and 3 components of the spin 4-vector, as above but for the step rather than at track endpoints.

```

<kswrite_root_condition_periodic name="condition_periodic"
group="component_step_world" parent="time" initial_min="0.9999"
initial_max="1.0001" increment="1." reset_min="0.499"
reset_max="0.501"/>

```

Finally, though this is not specific to UCNs, we note the addition of this write condition, which was useful to us. Write conditions in Kassiopeia restrict the output (in this case step output) to only occur when certain conditions are met.

This condition allows step output only if the time is within 0.0001 seconds of an integer number of seconds, and then disables the output until another step is within 0.001 seconds of a half-integer number of seconds. While this may sound bizarre, it allows a relatively general way to output only at (almost exactly) integer seconds, which is independent of individual integration step sizes as long as they are sufficiently small. This was used in order to keep our output files at a manageable length.

Appendix B

Figures

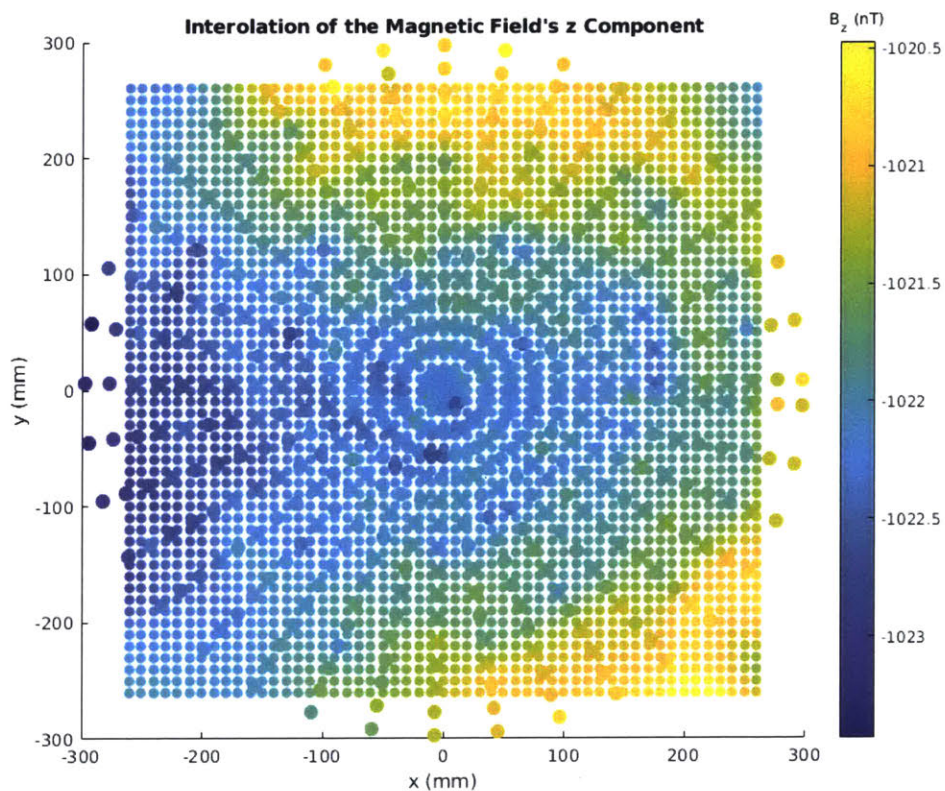


Figure B-1: A plot of the z component of the magnetic field at the center (length-wise) of the PSI precession chamber in one of the field configurations. The larger dots are the field values provided to us (measured in [39]) while the smaller dots are our interpolated values. The $\mathcal{O}(1 \text{ nT})$ variations in the field are typical of the entire trap, both configurations, and all three components.

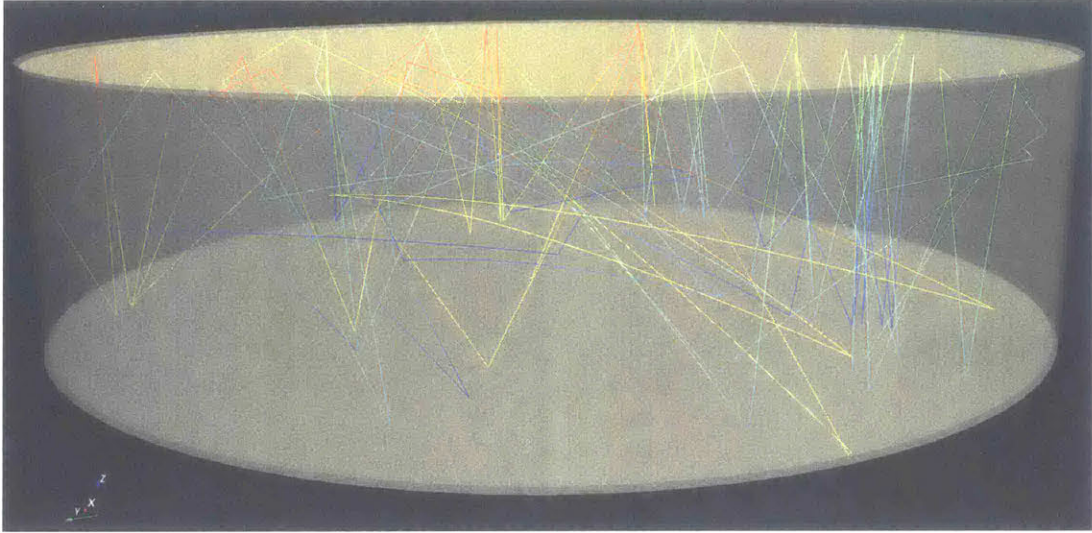


Figure B-2: A VTK image of three neutrons tracked for 1 second inside of the PSI precession chamber. Colors correspond to kinetic energies, with higher energies at the blue end of the spectrum. Note the approximately specular reflections and the slight curvature in the tracks induced by gravity.

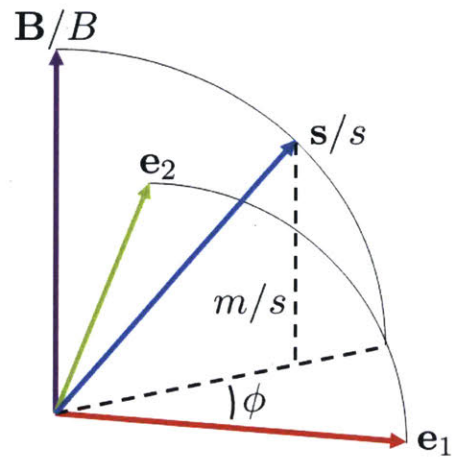


Figure B-3: The vectors used to define the adiabatic coordinates m and ϕ from the spin vector \mathbf{s} in (3.5).

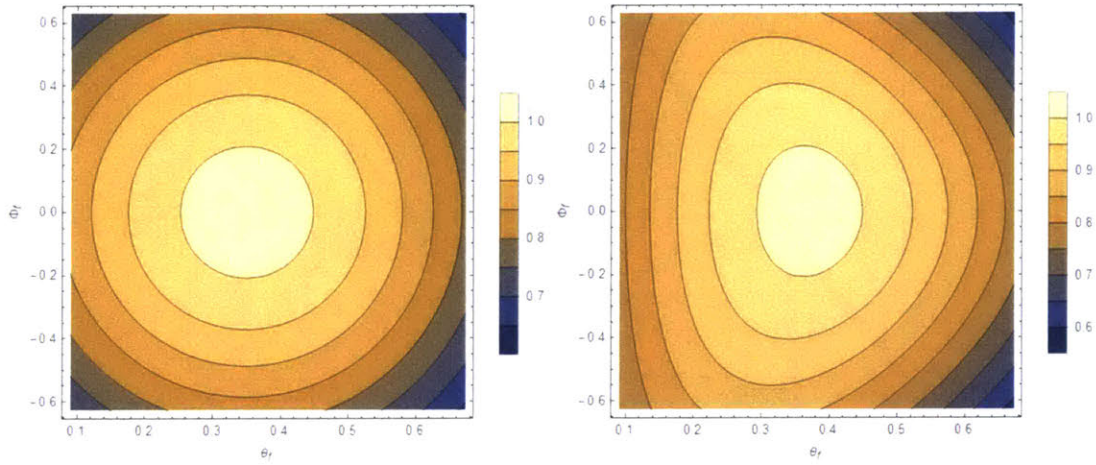


Figure B-4: Plots of the exact (left, see (4.2)) and approximate (right, see (4.4b)) outgoing angle distributions for a UCN incident on a surface with $wk = 2.4$ (typical for our simulations) and an angle to the surface normal of $\pi/7$. Note how the two distributions are reasonably similar, though the approximation is rough since $wk \sim 1$. This was acceptable for us since there was no reason for our simulation results to depend strongly on the exact angular distribution function.

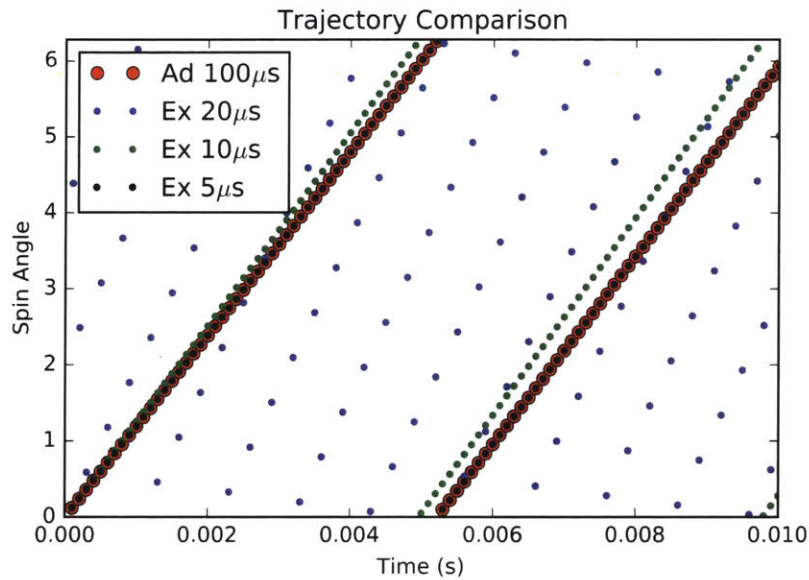


Figure B-5: A comparison of neutron spin angles around the local magnetic field (in the coordinate system defined by (3.5)), including an adiabatic trajectory with an integration time step of $100 \mu\text{s}$ and exact trajectories with time steps of 5, 10, and $20 \mu\text{s}$. These were run in a version of the neutron precession chamber described in this work, but with the magnetic field scaled up by a factor of 1000, resulting in a precession frequency of approximately 30 MHz. As this comparison shows, the adiabatic trajectory agrees well with the exact trajectory at a much shorter step size, but the exact trajectory rapidly loses accuracy as the step size approaches the precession period of $33 \mu\text{s}$. Note that the plot necessarily suffers from aliasing, but sampling was done simultaneously so that points at the same time can be compared.

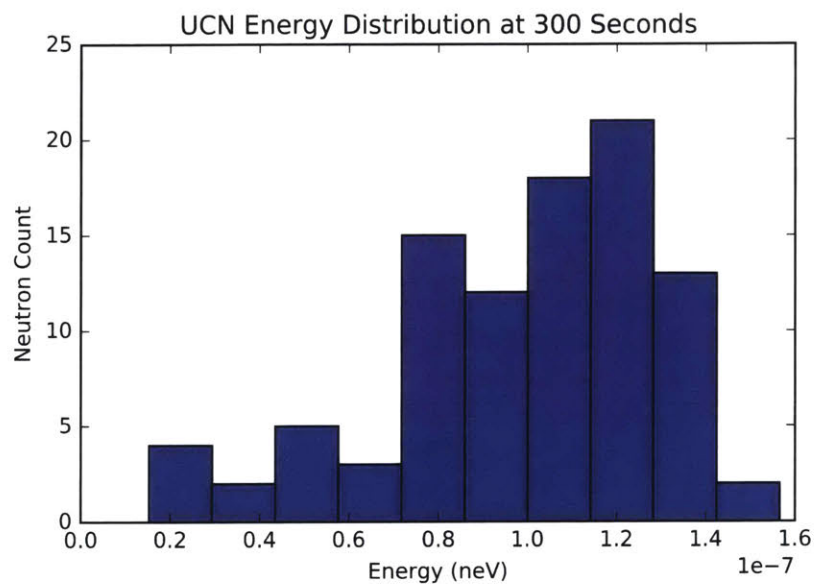


Figure B-6: The distribution of UCN energies after 300 seconds, using adiabatic simulations of neutrons in one field configuration. Note that the average energy is now far below the initial 150 neV, and in fact a sharp cutoff around the real part of the optical potential (approximately 150 neV) is apparent.

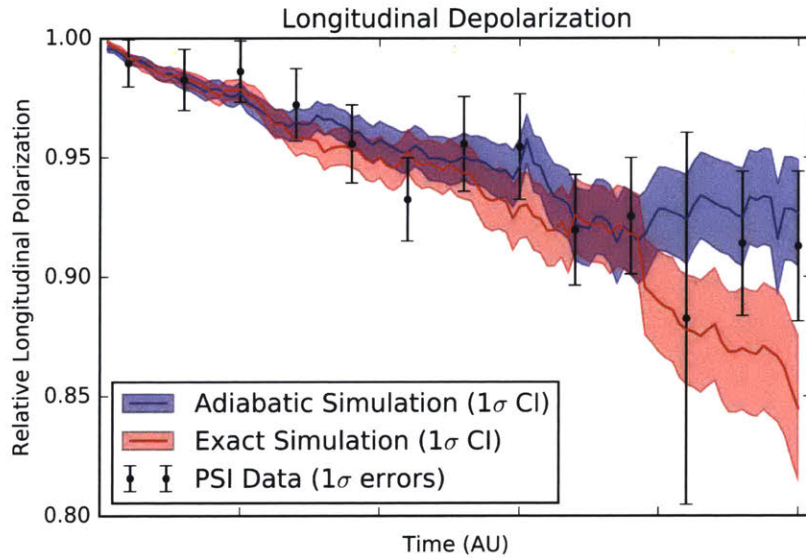


Figure B-7: A comparison of the fractional remaining longitudinal polarization measured at PSI (Figure 5.18 in [23], p.114) with the results of our adiabatic and exact simulations, including 1σ confidence intervals for the simulations and 1σ error bars for the experimental data. The x-axis labels are hidden as the PSI data sets are not yet published. Here, a 0.95 relative polarization corresponds to an average spin along the z-axis equal to 0.95 times the initial average spin along the z-axis. Each data set averages over the two field configurations and over initially aligned and anti-aligned neutrons. We see good agreement over the entire period; the deviation of the exact data at long times is not statistically significant.

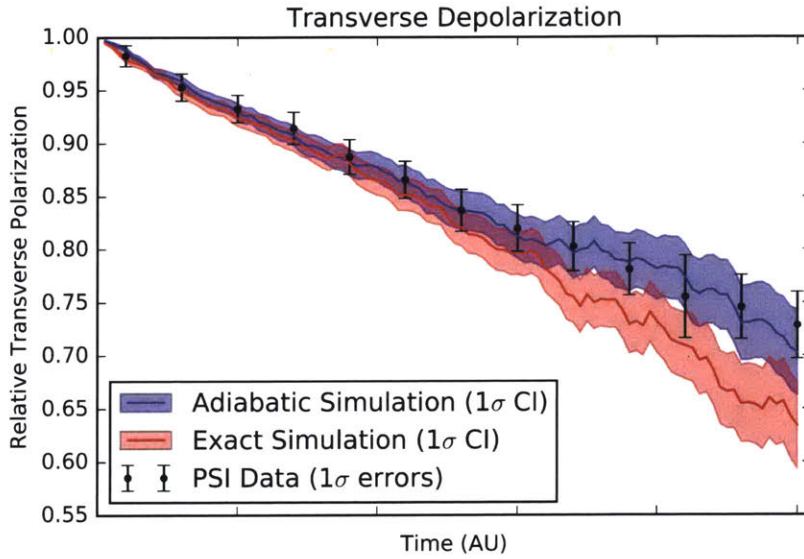


Figure B-8: A comparison of the fractional remaining transverse polarization measured at PSI (Figure 2.38 in [42], p.73) with the results of our adiabatic and exact simulations, including 1σ confidence intervals for the simulations and 1σ error bars for the experimental data. The x-axis labels are hidden as the PSI data sets are not yet published. Here, a 0.95 relative polarization corresponds to an average spin along the axis of average precession equal to 0.95 times the initial average spin along the initial polarization axis. Each data set averages over the two field configurations and over two initial spin directions. We see good agreement over the entire period; the deviation of the exact data at long times is not statistically significant.

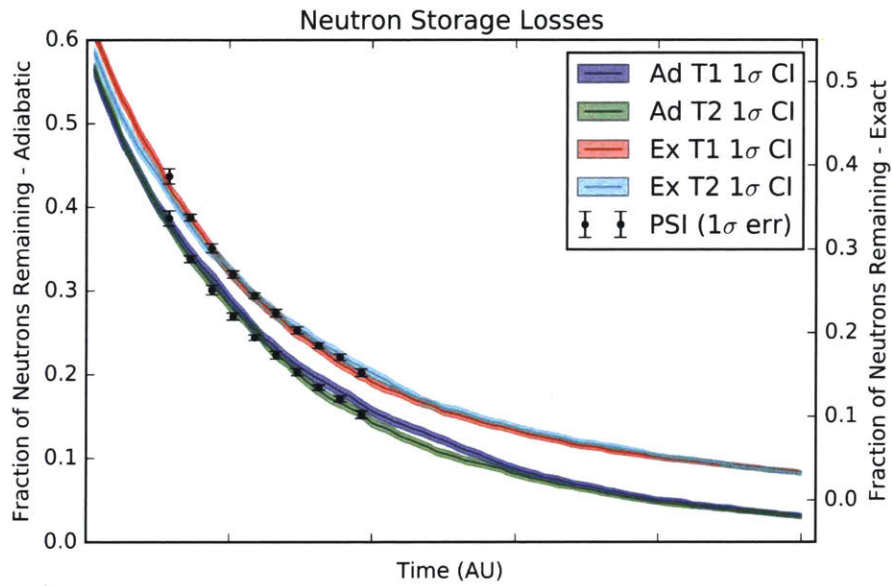


Figure B-9: A comparison of the fraction of neutrons remaining in the trap measured at PSI (Figure 2.37 in [42], p.72) with the results of our adiabatic and exact simulations, including 1σ confidence intervals for the simulations and 1σ error bars for the experimental data. The x-axis labels are hidden as the PSI data sets are not yet published. Averages for each data set are taken as in Figure B-7 and Figure B-8. Good agreement is seen along the entire PSI data set. Note that the exact data uses a shifted y-axis for visual clarity. The experimental values are arbitrarily normalized as the initial neutron count is not known.

Appendix C

Tables

Simulation	T1 or T2		Lifetime	
	χ^2/ndf	p	χ^2/ndf	p
T1 Ad	0.22	1.00	2.43	0.02
T1 Ex	0.66	0.84	0.53	0.90
T2 Ad	0.13	1.00	0.56	0.88
T2 Ex	1.29	0.29	0.85	0.66

Table C.1: The results of χ^2 testing of our results against the PSI experimental data, including left-sided p-values. Note that $\text{ndf}=11$ for the T1 and T2 measurements and $\text{ndf}=9$ for the lifetime measurements. These values suggest that we are over-estimating our errors, likely due to our results being strongly correlated. The T1 adiabatic lifetime data's disagreement with the experimental data may indicate that our assumed value of η was not correct.

Bibliography

- [1] C. Abel et al. Search for axionlike dark matter through nuclear spin precession in electric and magnetic fields. *Phys. Rev. X*, 7:041034, Nov 2017.
- [2] C. Abel et al. nEDM experiment at PSI: data-taking strategy and sensitivity of the dataset. In *International Workshop on Particle Physics at Neutron Sources 2018 (PPNS 2018) Grenoble, France, May 24-26, 2018*, 2018.
- [3] C. Abel et al. Statistical sensitivity of the nEDM apparatus at PSI to neutron mirror-neutron oscillations. In *International Workshop on Particle Physics at Neutron Sources 2018 (PPNS 2018) Grenoble, France, May 24-26, 2018*, 2018.
- [4] S. Afach et al. A device for simultaneous spin analysis of ultracold neutrons. *The European Physical Journal A*, 51(11):143, Nov 2015.
- [5] S. Afach et al. Observation of gravitationally induced vertical striation of polarized ultracold neutrons by spin-echo spectroscopy. *Phys. Rev. Lett.*, 115:162502, Oct 2015.
- [6] J. Allison et al. Recent developments in geant4. *Nuclear Instruments and Methods in Physics Research Section A: Accelerators, Spectrometers, Detectors and Associated Equipment*, 835:186 – 225, 2016.
- [7] I. Altarev et al. New constraints on lorentz invariance violation from the neutron electric dipole moment. *EPL (Europhysics Letters)*, 92(5):51001, 2010.
- [8] F. Atchison et al. Cold neutron energy dependent production of ultracold neutrons in solid deuterium. *Phys. Rev. Lett.*, 99:262502, Dec 2007.
- [9] F. Atchison et al. Loss and spinflip probabilities for ultracold neutrons interacting with diamondlike carbon and beryllium surfaces. *Phys. Rev. C*, 76:044001, Oct 2007.
- [10] F. Atchison et al. Diffuse reflection of ultracold neutrons from low-roughness surfaces. *The European Physical Journal A*, 44(1):23–29, Apr 2010.
- [11] Nicholas J. Ayres et al. *Monte Carlo Simulations for the Optimization and Data Analysis of Experiments with Ultracold Neutrons*. 2018.

- [12] C. A. Baker et al. Improved experimental limit on the electric dipole moment of the neutron. *Phys. Rev. Lett.*, 97:131801, Sep 2006.
- [13] C. A. Baker et al. Apparatus for Measurement of the Electric Dipole Moment of the Neutron using a Cohabiting Atomic-Mercury Magnetometer. *Nucl. Instrum. Meth.*, A736:184–203, 2014.
- [14] J. Baron et al. Order of magnitude smaller limit on the electric dipole moment of the electron. *Science*, 343(6168):269–272, 2014.
- [15] John Patrick Barrett. *A Spatially Resolved Study of the KATRIN Main Spectrometer Using a Novel Fast Multipole Method*. PhD thesis, Massachusetts Institute of Technology, 2 2017.
- [16] R. Brun and F. Rademakers. ROOT: An object oriented data analysis framework. *Nucl. Instrum. Meth.*, A389:81–86, 1997.
- [17] Svetlana Chesnevskaya. *Investigation of electric fields, losses and depolarization of ultra-cold neutrons for the new nEDM experiment at FRM II*. PhD thesis, Technical University of Munich, 1 2015.
- [18] B. Clément and D. Roulier. Starucn. <https://sourceforge.net/projects/starucn/>, 2014. Accessed: 2018-10-10.
- [19] Thomas Joseph Corona. Tools for electromagnetic field simulation in the katrin experiment. Master’s thesis, Massachusetts Institute of Technology, 2 2009.
- [20] Liu Dongping, Liu Yanhong, and Chen Baoxiang. Surface roughness of various diamond-like carbon films. *Plasma Science and Technology*, 8(6):701, 2006.
- [21] Ali Ashtari Esfahani et al. Determining the neutrino mass with cyclotron radiation emission spectroscopy—project 8. *Journal of Physics G: Nuclear and Particle Physics*, 44(5):054004, 2017.
- [22] Daniel Furse et al. Kassiopia: a modern, extensible c++ particle tracking package. *New Journal of Physics*, 19(5):053012, 2017.
- [23] Victor Helaine. *Neutron Electric Dipole Moment measurement: simultaneous spin analysis and preliminary data analysis*. PhD thesis, Université de Caen, 9 2014.
- [24] J. J. Hudson et al. Improved measurement of the shape of the electron. *Nature*, 473:493 – 496, May 2011.
- [25] J. D. Jackson. *Classical Electrodynamics*. John Wiley & Sons Inc., 3 edition, 1999.

- [26] Bernhard Lauss. Ultracold neutron production at the second spallation target of the paul scherrer institute. *Physics Procedia*, 51:98 – 101, 2014. ESS Science Symposium on Neutron Particle Physics at Long Pulse Spallation Sources, NPPatLPS 2013.
- [27] Robert G. Littlejohn and Stefan Weigert. Adiabatic motion of a neutral spinning particle in an inhomogeneous magnetic field. *Phys. Rev. A*, 48:924–940, Aug 1993.
- [28] Thomas Mannel. Theory and phenomenology of cp violation. *Nuclear Physics B - Proceedings Supplements*, 167:170 – 174, 2007. Proceedings of the 7th International Conference on Hyperons, Charm and Beauty Hadrons.
- [29] Pieter Mumm. Resolving the neutron lifetime puzzle. *Science*, 360(6389):605–606, 2018.
- [30] J. M. Pendlebury et al. Revised experimental upper limit on the electric dipole moment of the neutron. *Phys. Rev. D*, 92:092003, Nov 2015.
- [31] J. M. Pendlebury et al. Revised experimental upper limit on the electric dipole moment of the neutron. *Phys. Rev. D*, 92:092003, Nov 2015.
- [32] A. Pichlmaier, V. Varlamov, K. Schreckenbach, and P. Geltenbort. Neutron lifetime measurement with the ucn trap-in-trap mambo ii. *Physics Letters B*, 693(3):221 – 226, 2010.
- [33] W. Schreyer et al. Pentrack—A simulation tool for ultracold neutrons, protons, and electrons in complex electromagnetic fields and geometries. *Nuclear Instruments and Methods in Physics Research Section A: Accelerators, Spectrometers, Detectors and Associated Equipment*, 858:123 – 129, 2017.
- [34] W. Schroeder, K. Martin, and B. Lorensen. *The Visualization Toolkit (4th Ed.)*. Kitware, 2006.
- [35] A. Steyerl. Measurements of total cross sections for very slow neutrons with velocities from 100 m/sec to 5 m/sec. *Physics Letters B*, 29(1):33 – 35, 1969.
- [36] A. Steyerl. Effect of surface roughness on the total reflexion and transmission of slow neutrons. *Zeitschrift für Physik A Hadrons and nuclei*, 254(2):169–188, Apr 1972.
- [37] Yuk-Hong Ting et al. Surface roughening of polystyrene and poly(methyl methacrylate) in ar/o2 plasma etching. *Polymers*, 2(4):649–663, 2010.
- [38] M. Wohlmuther and G. Heidenreich. The spallation target of the ultra-cold neutron source ucn at psi. *Nuclear Instruments and Methods in Physics Research Section A: Accelerators, Spectrometers, Detectors and Associated Equipment*, 564(1):51 – 56, 2006.

- [39] Grzegorz Wyszynski. *Development of Magnetic Field Control Systems in the nEDM Experiment*. PhD thesis, Jagiellonian University in Kraków, 2015.
- [40] A. T. Yue et al. Improved determination of the neutron lifetime. *Phys. Rev. Lett.*, 111:222501, Nov 2013.
- [41] Yakov Borisovich Zel'dovich. Storage of cold neutrons. *Soviet Physics Journal of Experimental & Theoretical Physics*, 9:1389, 1959.
- [42] Johannes Zenner. *The search for the neutron electric dipole moment*. PhD thesis, Johannes Gutenberg University Mainz, 8 2013.
- [43] G. Zsigmond. The mcucn simulation code for ultracold neutron physics. *Nuclear Instruments and Methods in Physics Research Section A: Accelerators, Spectrometers, Detectors and Associated Equipment*, 881:16 – 26, 2018.